

Supporting Information for  
**Weakening Indian Ocean carbon uptake in 2015: the role of  
amplified basin-wide warming and reduced Indonesian  
Throughflow**

Enhui Liao<sup>1\*</sup>, Wenfang Lu<sup>2</sup>, Liang Xue<sup>3</sup>, Yan Du<sup>4,5</sup>

<sup>1</sup>School of Oceanography, Shanghai Jiao Tong University, Shanghai, 200030, China

<sup>2</sup>School of Marine Sciences, Sun Yat-Sen University, And Southern Marine Science and Engineering Guangdong Laboratory (Zhuhai), Zhuhai, 519000, China

<sup>3</sup>First Institute of Oceanography, Ministry of Natural Resources, Qingdao, 266061, China

<sup>4</sup>State Key Laboratory of Tropical Oceanography, SCSIO, CAS, Guangzhou, 510300, China

<sup>5</sup>University of Chinese Academy of Sciences, Beijing, 100049, China

\*Correspondence to: [ehliao@sjtu.edu.cn](mailto:ehliao@sjtu.edu.cn)

Contents of this file

Section S1 Data and model evaluation

Section S2 Model setup

Section S3 Ocean CO<sub>2</sub> flux decomposition

Section S4 Ocean pCO<sub>2</sub> decomposition

Section S5 Ocean pCO<sub>2</sub> responses to IOD and ENSO

Section S6 Influence of Indonesian Throughflow on the ocean carbon cycle

Section S7 Fig. S1-S18

References

## Section S1 Data and model evaluation

The Research Moored Array for African-Asian-Australian Monsoon Analysis and Prediction (RAMA) is downloaded from the Pacific Marine Environmental Laboratory NOAA (McPhaden et al. 2009; Sutton et al. 2014). We use data from the RAMA moorings at 90°E, 15°N, 57°E, 4°S, and 95°E, 5°S. Other datasets used for model evaluation and analysis can be found in the Section S1 of supporting information.

Model and observation climatological fields are computed for the period spanning from January 1982 to December 2020, except when observations are covered by a shorter period; that is, satellite chlorophyll climatology is computed for 1997–2020. The anomaly is defined as the deseasonalized-interannual anomaly, which is computed by first removing the quadratic trend for the period from 1982 to 2020, then subtracting the 1982–2020 climatological monthly value, and finally filtered by a 3-month moving average filter. The Indian Ocean is defined as the region situated between 30°N–30°S, extending from the African coastline (30°E) to the Maritime coastline (120°E). The year an El Niño event begins is defined as the El Niño year. For instance, the El Niño event that commenced in the summer of 1997 and peaked between December 1997 and February 1998 is identified as El Niño 1997. This definition applies uniformly to other El Niño and La Niña events.

For model evaluation, chlorophyll, nitrate (NO<sub>3</sub>), phosphate (PO<sub>4</sub>), dissolved inorganic carbon (DIC), sea surface temperature (SST), sea surface salinity (SSS), and mixing layer depth (MLD) are selected to compare with observational data. The chlorophyll data is obtained from Ocean Colour Climate Change Initiative (OC-CCI) version 5.0 (Sathyendranath et al. 2019). The NO<sub>3</sub> and PO<sub>4</sub> are sourced from World Ocean Atlas version 2013, while the DIC data is from Global Ocean Data Analysis Project (GLODAP) v2 (Olsen et al. 2016). The SST data is acquired from the Optimum Interpolation SST (OISST) v2 (Banzon et al. 2016) and sea surface salinity (SSS) is from the Multi-Mission Optimum Interpolated Sea Surface Salinity Global Dataset (OISSS) (Melnichenko et al. 2021). The MLD data, based on a density criteria of 0.03 kg/m<sup>3</sup>, is sourced from de Boyer Montégut et al. (2004), while the thermocline depth (20°C depth) is computed from Argo gridded temperature data (Roemmich and Gilson 2009). The observed IOD indexes are computed using OISST. The SST anomaly for IOD computation is based on the mean in 1981–2010, following the methodology of the physical sciences laboratory from National Oceanic and Atmospheric Administration (NOAA, [https://psl.noaa.gov/gcos\\_wgsp/Timeseries/DMI/](https://psl.noaa.gov/gcos_wgsp/Timeseries/DMI/)).

Wind speed is obtained from Cross-Calibrated Multi-Platform (CCMP) v3.0 monthly wind product (Mears et al. 2022). The Indonesian throughflow volume transport is computed from global reanalysis ensemble product (GREP) (Storto et al. 2019) and ocean reanalysis system 5 (ORAS5) ocean products (Zuo et al. 2019).

Fig. S3 evaluates the climatological mean status of various oceanographic parameters, including SST, SSS, MLD, and Chlorophyll. The model underestimates the MLD in the southern Indian Ocean, which might be due to the weak JRA 55-do wind product or potentially inaccurate mixing computation scheme in the model. The model also underestimates the chlorophyll in the open ocean of Arabian Sea and Bay of Bengal which is potentially due to the less simulated nitrate and phosphate. Fig. S4 assesses the biogeochemical module (COBALT) by comparing observed and simulated DIC, alkalinity (Alk), NO<sub>3</sub>, and PO<sub>4</sub>. The model slightly overestimates the DIC and Alk in the southern Indian Ocean, while weakly underestimates the NO<sub>3</sub> and PO<sub>4</sub> in the Indian Ocean basin scale. In Fig. S5, the climatological mean air-sea CO<sub>2</sub> flux and ocean pCO<sub>2</sub> are evaluated using the OS-ETHZ-GRaCER and SOM-FFN products. Overall, the model demonstrates good agreement of the spatial distribution of ocean carbon-related tracers, including DIC, Alk, CO<sub>2</sub> flux, and ocean pCO<sub>2</sub>.

We assess the interannual anomaly of SST, SSS, and thermocline depth (depth of 20 °C) at two RAMA stations in the equatorial Indian Ocean (57°E-4°S and 95°E-5°S, Fig. S6) and ocean pCO<sub>2</sub> and ΔpCO<sub>2</sub> at one RAMA station in the Bay of Bengal (90°E-15°N, Fig. S7). The model accurately captures the anomalous timing and magnitude of these fields related to the IOD. Furthermore, we have compared all observed ocean pCO<sub>2</sub> from Surface Ocean CO<sub>2</sub> Atlas (SOCAT v2022) product (Bakker et al. 2016) in the Indian Ocean with model output through scatter plot (Fig. S1) and box plot (Fig. S8). In the SOCAT comparison, the simulated pCO<sub>2</sub> is adjusted to ocean CO<sub>2</sub> fugacity (fCO<sub>2</sub>) using a conversion coefficient. This coefficient is derived from Wanninkhof et al., (2020) and Weiss (1974) and the computation code is based on model the ocean carbonate system (mocsy) model (Orr and Epitalon 2015).

These evaluations indicate the model is capable of reproducing the spatial and temporal variability of ocean carbon cycle in the Indian Ocean. As a result, the model is considered trustworthy and reliable for studying the extreme air-sea CO<sub>2</sub> flux anomaly that occurred in 2015.

## **Section S2 Model setup**

The global ocean/sea ice model coupled with a biogeochemical module from the Geophysical Fluid Dynamics Laboratory (GFDL) is employed in this study. The physical model includes Modular Ocean Model version 6 (MOM6) and Sea Ice Simulator version 2 (SIS2). The version of the physical model adopted here is OM4P5 with a horizontal resolution of 0.5° and eddy parameterization (see the detailed configuration in Adcroft et al. (2019)). The coupled biogeochemical module is Carbon Ocean Biogeochemistry and Lower Trophics version 2 (COBALT v2), which encompasses 33 state variables: nutrients (nitrate, phosphate, silicate, and iron), oxygen, carbonate system, three phytoplankton groups, three zooplankton groups, three dissolved organic carbon pools, and one particulate detritus pool (Stock et al. 2020). Details about

planktonic food web dynamics within COBALT and global assessments of large-scale carbon fluxes through the food web can refer to Stock et al. (2020).

The ocean model is forced by the Japanese 55-year atmospheric reanalysis dataset (JRA55-do) version 1.5 (Tsujino et al. 2018) and atmospheric deposition data (iron, lithogenic material, PO<sub>4</sub>, wet and dry NO<sub>3</sub> and NH<sub>4</sub>) from GFDL-ESM4 models. The hindcast simulation is then performed from 1959 to 2020. The model performance is thoroughly assessed, and it reproduces well-observed physical and biogeochemical features in the Indian Ocean, including both climatological mean state and interannual variability. The accurately replicated climatological features include the east-west gradient of sea surface salinity, mixed-layer depth (MLD), dissolved inorganic carbon (DIC), alkalinity (Alk), and nutrients between the Arabian Sea and Bay of Bengal, as well as the north-south gradient of SST, chlorophyll, nutrients, ocean pCO<sub>2</sub>, and CO<sub>2</sub> flux between northern and southern Indian Ocean (Fig. S3-S5). The model demonstrates strong capability in capturing the interannual variability of SST, SSS, thermocline depth, and ocean pCO<sub>2</sub> at RAMA stations and SOCAT observational sites (Fig. S1, S6-S8). In addition, a simulation with a similar setup, driven by JRA55-do v1.3, was well evaluated and applied to examine the air-sea CO<sub>2</sub> flux variability in the Pacific Ocean. For more detailed configurations and evaluations of the model, readers can refer to Liao et al. (2020).

The model was spun up from rest for a period of 81 years by repeating the JRA55-do v1.5 forcing in the year of 1959. The atmospheric xCO<sub>2</sub> global average driving MOM6-COBALT2 is from global carbon budget project (Friedlingstein et al. 2022). The xCO<sub>2</sub> is a global average derived from monthly Mauna Loa Observatory (MLO) and South Pole Observatory (SPO) station data. For model initialization, temperature, salinity, nutrients (nitrate, phosphate, and silicate), and oxygen are sourced from World Ocean Atlas version 2013 (Garcia et al. 2013a; Garcia et al. 2013b; Locarnini et al. 2013; Zweng et al. 2013). The initial dissolved inorganic carbon (DIC) and alkalinity (Alk) are obtained from the GLODAP v2 (Olsen et al. 2016). The initial DIC is corrected for the accumulation of anthropogenic carbon to match the level expected in 1959 using the data-based estimate of ocean anthropogenic carbon content (Khatiwala et al. 2013). Other COBALT tracer initial conditions (e.g., ammonium, calcium carbonate) are taken from a preindustrial GFDL-ESM2M-COBALT simulation (Stock et al. 2014).

Note that the two data products in the Fig. 2a and 2b have slight differences in the years 1982-1984 and 1998, which might be due to data sparsity and variations in machine learning methods. The model simulates a larger CO<sub>2</sub> flux anomaly than the two data products in 1997-1998, which might be related to an overestimation of SST. However, the two data products might not entirely reflect true values due to limited data availability during that early period (1997-1998). Despite these slight discrepancies, the model still performs well in capturing the timing and magnitude of CO<sub>2</sub> flux interannual variability, as shown by the two data products in the Indian Ocean.

### Section S3 Ocean CO<sub>2</sub> flux decomposition

The air-sea CO<sub>2</sub> flux ( $FCO_2$ ) is computed using the following bulk formula:

$$FCO_2 = k_w \alpha (pCO_{2w} - pCO_{2a}) \quad (S1)$$

where  $pCO_{2a}$  is the atmospheric partial pressure of CO<sub>2</sub>,  $pCO_{2w}$  is the sea surface partial pressure of CO<sub>2</sub>,  $\alpha$  denotes CO<sub>2</sub> solubility, computed using the temperature and salinity dependent formulation of Weiss and Price (1980), and  $k_w$  is the CO<sub>2</sub> gas transfer coefficient computed by a quadratic wind-speed formulation (Wanninkhof 2014). The two coefficients computation follows Najjar and Orr (1998). The positive  $FCO_2$  denotes an oceanic outgassing of CO<sub>2</sub>.

Assuming  $\Delta pCO_2 = pCO_{2w} - pCO_{2a}$  and  $k_w \alpha = K$ , the Equation S1 becomes:

$$FCO_2 = K \Delta pCO_2 \quad (S2)$$

When the seasonality and quadratic trend are removed,  $FCO_2$ ,  $K$ , and  $\Delta pCO_2$  can be decomposed into a component from interannual anomaly ( $FCO'_2$ ,  $K'$ , and  $\Delta pCO'_2$ ) and a component from long-term mean ( $\overline{FCO_2}$ ,  $\bar{K}$ , and  $\overline{\Delta pCO_2}$ ). The relationship between them is shown as:  $FCO_2 = FCO'_2 + \overline{FCO_2}$ ,  $K = K' + \bar{K}$ , and  $\Delta pCO_2 = \Delta pCO'_2 + \overline{\Delta pCO_2}$ . The effect of  $K$  and  $\Delta pCO_2$  on air-sea CO<sub>2</sub> flux interannual variations ( $FCO'_2$ ) is able to be isolated by a linear Taylor expansion following a similar method to a previous study (Doney et al. 2009):

$$\begin{aligned} FCO_2 &= K \Delta pCO_2 = (K' + \bar{K})(\Delta pCO'_2 + \overline{\Delta pCO_2}) \\ FCO_2 &= K' \Delta pCO'_2 + \bar{K} \Delta pCO'_2 + K' \overline{\Delta pCO_2} + \bar{K} \overline{\Delta pCO_2} \end{aligned}$$

The long-term mean  $\overline{FCO_2}$  can be expressed as:

$$\overline{FCO_2} = \langle FCO_2 \rangle = \langle K' \Delta pCO'_2 + \bar{K} \Delta pCO'_2 + K' \overline{\Delta pCO_2} + \bar{K} \overline{\Delta pCO_2} \rangle \quad (S3)$$

where we use angle brackets to denote the average. Using Equations S2- S3 yields:

$$\begin{aligned} FCO'_2 &= FCO_2 - \overline{FCO_2} \\ FCO'_2 &= K' \Delta pCO'_2 + \bar{K} \Delta pCO'_2 + K' \overline{\Delta pCO_2} + \bar{K} \overline{\Delta pCO_2} \\ &\quad - \langle K' \Delta pCO'_2 + \bar{K} \Delta pCO'_2 + K' \overline{\Delta pCO_2} + \bar{K} \overline{\Delta pCO_2} \rangle \\ FCO'_2 &= \bar{K} \overline{\Delta pCO_2} - \langle \bar{K} \overline{\Delta pCO_2} \rangle + \bar{K} \Delta pCO'_2 - \langle \bar{K} \Delta pCO'_2 \rangle + K' \overline{\Delta pCO_2} - \langle K' \overline{\Delta pCO_2} \rangle \\ &\quad + K' \Delta pCO'_2 - \langle K' \Delta pCO'_2 \rangle \end{aligned}$$

Assuming the interannual anomaly is randomly distributed and we have:

$$\begin{aligned} \langle \bar{K} \overline{\Delta pCO_2} \rangle &= \bar{K} \overline{\Delta pCO_2} \\ \langle \bar{K} \Delta pCO'_2 \rangle &= \bar{K} \langle \Delta pCO'_2 \rangle = \bar{K} \cdot 0 = 0 \end{aligned}$$

$$\langle K' \overline{\Delta p CO_2} \rangle = \langle K' \rangle \overline{\Delta p CO_2} = 0 \cdot \overline{\Delta p CO_2} = 0$$

$$\langle K' \Delta p CO_2' \rangle = \langle K' \Delta p CO_2' \rangle$$

This yields:

$$FCO_2' = \bar{K} \Delta p CO_2' + K' \overline{\Delta p CO_2} + (K' \Delta p CO_2' - \langle K' \Delta p CO_2' \rangle) \quad (S4)$$

$$FCO_2' = \bar{K} \Delta p CO_2' + K' \overline{\Delta p CO_2} + RES \quad (S5)$$

where RES is the small residual of the cross terms ( $K' \Delta p CO_2' - \langle K' \Delta p CO_2' \rangle$ ).

Equation S5 illustrates that the CO<sub>2</sub> flux anomaly ( $FCO_2'$ ) is affected by three components:  $\Delta p CO_2$  anomaly ( $\bar{K} \Delta p CO_2'$ ), gas transfer coefficient anomaly ( $K' \overline{\Delta p CO_2}$ ), and a small residual term ( $RES$ ) which results from the cross terms ( $K' \Delta p CO_2' - \overline{K' \Delta p CO_2'}$ ).

This framework has been widely used in various prior studies, focusing on the global ocean and tropical Pacific Ocean and coastal ocean (Doney et al. 2009; McKinley et al. 2004; Obata and Kitamura 2003). In our study, based on our model results, we found interannual variations in the air-sea CO<sub>2</sub> partial pressure difference ( $\Delta p CO_2$ ) explain 76.6% of the FCO<sub>2</sub> interannual variance in the Indian Ocean (Equation S5). The temporal changes in wind-solubility coefficient explain 28.1% of the FCO<sub>2</sub> interannual variance. Furthermore, we reveal that variations in  $pCO_{2w}$  accounted for 92.5% of the  $\Delta p CO_2$  variance in the tropical Pacific Ocean, while  $pCO_{2a}$  only accounted for less than 1%. This is consistent with the fact that the ocean surface  $pCO_2$  variability on interannual time-scale can be up to 50 times larger than the atmospheric CO<sub>2</sub> variability.

#### Section S4 Ocean $pCO_2$ decomposition

We quantify the driving processes of ocean  $pCO_2$  ( $pCO_{2w}$ ) by expanding a traditional ocean  $pCO_2$  decomposition framework to include all contributions from physical (advection, mixing, freshwater and thermal fluxes) and biological (photosynthesis and remineralization) processes. The traditional decomposition framework links variations in ocean  $pCO_2$  to changes in DIC, Alk, temperature and salinity using the following linear decomposition (Le Quéré et al. 2000; Takahashi et al. 1993):

$$\Delta p CO_{2w} \approx \frac{\partial p CO_{2w}}{\partial DIC} \Delta DIC + \frac{\partial p CO_{2w}}{\partial Alk} \Delta Alk + \frac{\partial p CO_{2w}}{\partial T} \Delta SST + \frac{\partial p CO_{2w}}{\partial S} \Delta SSS \quad (S6)$$

where  $\Delta$  is defined as temporal change of tracer ( $pCO_{2w}$ , DIC, Alk, T, and S) in this section. The tracer is defined as the mean value in the mixed-layer depth (depth where the water density is 0.01 kg/m<sup>3</sup> denser than the surface water). T and S denote the sea surface temperature and salinity respectively. Note that  $\Delta p CO_{2w}$  is the temporal change of ocean  $pCO_2$  and the  $\Delta p CO_2$  in section S3 is defined as ocean-atmospheric  $pCO_2$  difference. The Equation S6 is separated into the thermal component ( $pCO_{2w-T}$ ) and non-thermal component ( $pCO_{2w-NONT}$ ):

$$\Delta pCO_{2w-T} = \frac{\partial pCO_{2w}}{\partial T} \Delta T \quad (S7)$$

$$\Delta pCO_{2w-NONT} = \frac{\partial pCO_{2w}}{\partial DIC} \Delta DIC + \frac{\partial pCO_{2w}}{\partial Alk} \Delta Alk + \frac{\partial pCO_{2w}}{\partial S} \Delta S \quad (S8)$$

The temporal change in  $\Delta pCO_{2w-NONT}$  can be expressed as a function of temporal changes in DIC, Alk, and salinity.

$$\partial_t pCO_{2w-NONT} = \frac{\partial pCO_{2w}}{\partial DIC} \partial_t DIC + \frac{\partial pCO_{2w}}{\partial Alk} \partial_t Alk + \frac{\partial pCO_{2w}}{\partial S} \partial_t S \quad (S9)$$

Temporal changes in DIC, Alk, and S are controlled by ocean physical transport, biological processes and air-sea fluxes as follows:

$$\partial_t DIC = DIC_H + DIC_V + DIC_{FCO_2} + DIC_{Bio} + DIC_{FW} \quad (S10)$$

$$\partial_t Alk = Alk_H + Alk_V + Alk_{Bio} + Alk_{FW} \quad (S11)$$

$$\partial_t S = S_H + S_V + S_{FW} \quad (S12)$$

where the subscript  $H$  denotes the contribution from horizontal transport (advection and diffusivity in the meridional and zonal directions),  $V$  denotes the contribution from vertical transport (vertical advection and diffusivity),  $Bio$  denotes the DIC and Alk changes induced by biological processes (photosynthesis, respiration, calcium carbonate dissolution/precipitation, denitrification and nitrification),  $Q$  denotes the effect of surface heat flux,  $FW$  denotes the effect of freshwater fluxes (i.e., precipitation, evaporation, river and sea-ice melt), and  $DIC_{FCO_2}$  denotes the DIC change induced by air-sea  $CO_2$  flux.

Combining Equations S9-S12 yields:

$$\begin{aligned} \partial_t pCO_{2w-NONT} &\approx \frac{\partial pCO_{2w}}{\partial DIC} (DIC_H + DIC_V + DIC_{FCO_2} + DIC_{Bio} + DIC_{FW}) \\ &+ \frac{\partial pCO_{2w}}{\partial Alk} (Alk_H + Alk_V + Alk_{Bio} + Alk_{FW}) \\ &+ \frac{\partial pCO_{2w}}{\partial S} (S_H + S_V + S_{FW}) \end{aligned} \quad (S13)$$

We rearrange the terms of Equation S13 to isolate the temporal changes in  $pCO_{2w-nont}$  (time tendency referred to as the  $pCO_2$  response) on the left hand side (LHS), and the five terms that control the time tendency of  $pCO_{2w-nont}$  on the right-hand side (RHS):

$$\begin{aligned} \underbrace{(\partial_t pCO_{2w-nont})}_{pCO_2 \text{ response}} &\approx \underbrace{\left( \frac{\partial pCO_{2w}}{\partial DIC} DIC_H + \frac{\partial pCO_{2w}}{\partial Alk} Alk_H + \frac{\partial pCO_{2w}}{\partial S} S_H \right)}_{H_{Circ}} \\ &+ \underbrace{\left( \frac{\partial pCO_{2w}}{\partial DIC} DIC_V + \frac{\partial pCO_{2w}}{\partial Alk} Alk_V + \frac{\partial pCO_{2w}}{\partial S} S_V \right)}_{V_{Circ}} \end{aligned}$$

$$\begin{aligned}
& + \underbrace{\left( \frac{\partial pCO_{2w}}{\partial DIC} DIC_{FW} + \frac{\partial pCO_{2w}}{\partial Alk} Alk_{FW} + \frac{\partial pCO_{2w}}{\partial S} S_{FW} \right)}_{FW} \\
& + \underbrace{\left( \frac{\partial pCO_{2w}}{\partial DIC} DIC_{Bio} + \frac{\partial pCO_{2w}}{\partial Alk} Alk_{Bio} \right)}_{Bio} + \underbrace{\left( \frac{\partial pCO_{2w}}{\partial DIC} DIC_{FCO_2} \right)}_{Flux\ response}
\end{aligned} \tag{S14}$$

The five terms (units: uatm/s) on the RHS are the horizontal and vertical transport of dissolved species, i.e., DIC, Alk and salinity ( $H_{Circ}$  and  $V_{Circ}$ ), the dilution/concentration effect induced by freshwater fluxes and evaporation ( $FW$ ), the biological effect due to photosynthesis, respiration, calcium carbonate dissolution/precipitation, denitrification and nitrification ( $Bio$ ), the  $CO_2$  flux driven by the atmosphere-ocean  $pCO_2$  difference. By considering these five terms, Equation S14 provides a comprehensive understanding of how various physical and biogeochemical processes influence the temporal changes in the ocean  $pCO_2$  non-thermal component. This helps in deciphering the complex interactions and feedback mechanisms between different processes.

Following the same method, the temporal change in  $\Delta pCO_{2w-T}$  can be expressed as a function of temporal changes in T and is further expressed as a function of three driving processes.

$$\partial_t T = T_H + T_V + T_Q \tag{S15}$$

$$\partial_t pCO_{2w-T} \approx \frac{\partial pCO_{2w}}{\partial T} (T_H + T_V + T_Q) \tag{S16}$$

$$\partial_t pCO_{2w-T} \approx \underbrace{\left( \frac{\partial pCO_{2w}}{\partial T} T_H \right)}_{T_{Hcirc}} + \underbrace{\left( \frac{\partial pCO_{2w}}{\partial T} T_V \right)}_{T_{Vcirc}} + \underbrace{\left( \frac{\partial pCO_{2w}}{\partial T} T_Q \right)}_{T_{flux}} \tag{S17}$$

The Equation S17 provides a comprehensive understanding of how temperature variations are influenced by different processes (i.e., horizontal and vertical transports and surface heat flux), allowing us to better interpret the changes in the thermal component of ocean  $pCO_2$  over time. A temporal change of ocean  $pCO_2$  thermal component ( $pCO_2$ -T tendency) is driven by three processes: horizontal and vertical transport of temperature ( $TH_{circ}$  and  $TV_{circ}$ ) and surface heat flux ( $T_{flux}$ ).

The coefficients used for the  $pCO_{2w}$  dependence on DIC, Alkalinity, temperature, and salinity are approximated by the following equations (Lovenduski et al. 2007; Sarmiento and Gruber 2006):

$$\frac{\partial pCO_{2w}}{\partial DIC} \approx \frac{\overline{pCO_{2w}}}{\overline{DIC}} \frac{3 \times \overline{Alk} \times \overline{DIC} - 2 \times \overline{DIC}^2}{(2 \times \overline{DIC} - \overline{Alk})(\overline{Alk} - \overline{DIC})} \tag{S18}$$

$$\frac{\partial pCO_{2w}}{\partial Alk} \approx - \frac{\overline{pCO_{2w}}}{\overline{Alk}} \frac{\overline{Alk}^2}{(2 \times \overline{DIC} - \overline{Alk})(\overline{Alk} - \overline{DIC})} \tag{S19}$$

$$\frac{\partial pCO_{2w}}{\partial T} \approx \overline{pCO_{2w}} \times 0.0423 \tag{S20}$$

$$\frac{\partial pCO_{2w}}{\partial S} \approx \frac{\overline{pCO_{2w}}}{\overline{S}} \tag{S21}$$

where overbar denotes 1982-2020 annual means. The coefficients are time invariant. Coefficients for DIC and salinity (Equations S18 and S21) are positive, i.e.,  $p\text{CO}_{2w}$  increases with DIC and salinity, while the coefficient for alkalinity (Equation S19) is negative, i.e.,  $p\text{CO}_{2w}$  decreases with increasing alkalinity. The effects of DIC and Alk are often competing in changing  $p\text{CO}_{2w}$ , but the DIC effect generally dominates because the absolute value of the DIC coefficient is larger than the alkalinity coefficient in most regions of the ocean including the Indian Ocean (Takahashi et al. 1993).

The terms in Equations 2-4 are computed in the mixed layer depth, which is defined as depth where the water density is  $0.01 \text{ kg/m}^3$  denser than the surface water.

### **Section S5 Ocean $p\text{CO}_2$ responses to IOD and ENSO**

The impact of the IOD and El Niño on the ocean  $p\text{CO}_2$  are examined in the type of pure positive IOD (2019), pure El Niño (1991), combined positive IOD and El Niño (1997, 2015) in the Fig. S10. The classification refers to Nino3.4 and IOD index in the Fig. 2 and references from Aparna et al., (2012) and Guo et al., (2015). The year an El Niño event begins is defined as the El Niño year. As shown in Fig. S11, the ocean  $p\text{CO}_2$  in pure IOD (2019) is characterized as a high anomaly in the eastern Indian Ocean and a low anomaly in the western and central Indian Ocean. Under the influence of a pure El Niño, the ocean  $p\text{CO}_2$  is featured as high anomalies in both eastern and western Indian Oceans. The ocean  $p\text{CO}_2$  pattern during the combined IOD and El Niño in 1997 resembles the pattern in pure IOD (2019). The ocean  $p\text{CO}_2$  during combined IOD and El Niño in 2015 looks like the pattern in pure El Niño (1991), with high anomalies in both the eastern and western Indian Oceans. A significant distinction in 2015 is the larger amplitude of ocean  $p\text{CO}_2$  anomaly compared to that in 1991. Temperature effect ( $p\text{CO}_2\text{-T}$ ) in 2015 covers a much broader area of positive value than that in 1991 and other events. Non-temperature effect in 2015 extends further southward compared to other events.

Note that the classification of above event is based on ENSO and IOD occurrence (pure IOD, pure El Niño, combined IOD and El Niño). The classification can also be based on the peak time and duration of sea surface temperature (SST) anomaly: Normal IOD (develop and mature in Sep, Oct, and Nov), prolonged IOD (peak time is later), Unseasonable IOD (develop and mature in other months). Another classification is based on the spatial pattern of SST anomaly: Symmetrical (similar amplitude of warming and cooling anomaly between east and west Indian Ocean) and Asymmetrical (uneven amplitude of warming and cooling anomaly between east and west Indian Ocean).

### **Section S6 Influence of Indonesian Throughflow on the ocean carbon cycle**

In the climatological mean state, the Indonesian Throughflow (ITF) brings relatively fresh water from the Pacific Warm Pool to the Indian Ocean, leading to a dilution of DIC, Alk, and salinity and subsequently reducing the ocean  $p\text{CO}_2$  in the southeastern Indian Ocean (Feng et al. 2018; Hu et al. 2019). However, the dilution effect is reversed through a weakened volume transport of ITF (Fig. S16) and an increased ocean  $p\text{CO}_2$  in the Warm Pool region (west equatorial Pacific Ocean, Fig. S17) during 2015. This reversal is linked to the co-occurrence of positive IOD and extraordinary El Niño in 2015. As indicated by Fritz et al., (2023), the ITF volume transport in 2015 is the weakest since 1993. The extraordinary ITF volume transport might be the reason for the unique ocean  $p\text{CO}_2$  response in the southeastern Indian Ocean. The critical effect of ITF on the southeastern Indian Ocean carbon cycle in 2015 is consistent with findings from previous research that examined ITF pathway interannual variability (Valsala and Maksyutov 2010; Valsala et al. 2010).

The weakened ITF volume transport is induced by a reduced sea level difference between the Pacific and Indian Oceans, resulting from the eastward movement of the Warm Pool in the 2015 El Niño (Mayer et al. 2018). The departure of Warm Pool and related reduced rainfall increases surface DIC, alkalinity, and salinity, leading to a rise in ocean  $p\text{CO}_2$  in the Warm Pool region (Fig. S17). A further investigation reveals that the reversed dilution effect is largely driven by ocean  $p\text{CO}_2$  anomaly rather than the volume transport anomaly (Fig. S18). This suggests the ITF transports anomalous high ocean  $p\text{CO}_2$  water to the Indian Ocean, leading to an anomalous ocean carbon outgassing in 2015. It is noteworthy that the ocean carbon response to the ITF is consistent with previous findings related to salinity, which also suggests the significance of ITF horizontal transport in determining the high salinity anomaly in the southeastern Indian Ocean during a positive IOD (Kido and Tozuka 2017; Zhang et al. 2016). The influence of changed ITF on the carbon cycle in the Indian Ocean further reflects a remote effect of El Niño from the Pacific Ocean.

## **Section S7 Figs. S1-S18**

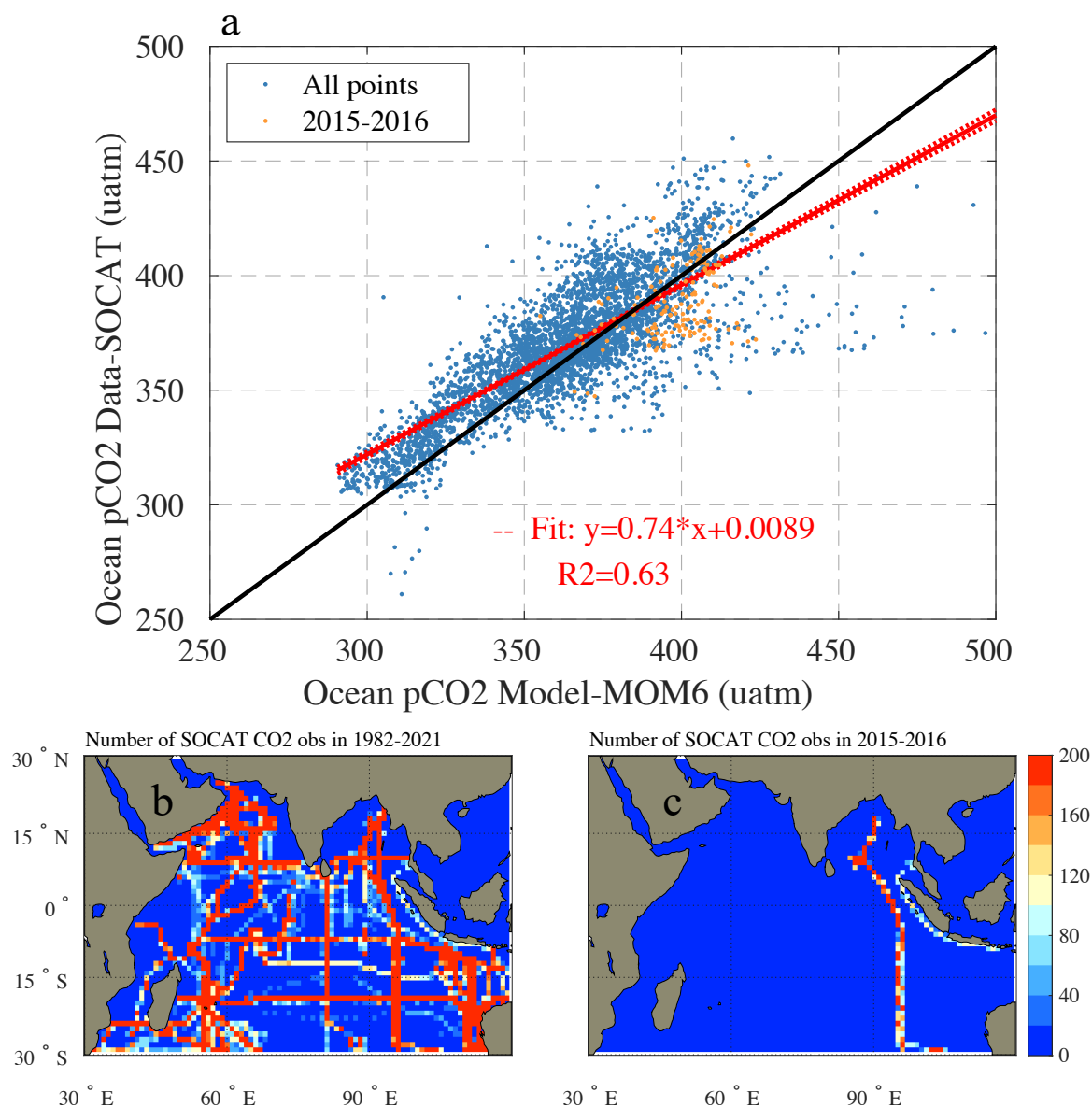


Fig. S1. Comparison of observed and simulated surface ocean CO<sub>2</sub> fugacity (fCO<sub>2</sub>) in the Indian Ocean during 1982-2020 (a), spatial distribution of number of SOCAT observation points in 1982-2020 (b) and 2015-2016 (c). The observed ocean CO<sub>2</sub> fugacity is collected from SOCAT monthly database. The simulated ocean pCO<sub>2</sub> is adjusted to fCO<sub>2</sub> and interpolated to match the SOCAT observation locations and times. a, the black line is the 1-to-1 line and the red line is regression line between data and model. The yellow dot in panel a indicates the point observed in August 2015 - August 2016 when IOD occurred. Shading in panel b and c indicates the number of SOCAT observation points. In panel c, the SOCAT cruise lines are observed in April and May 2016.

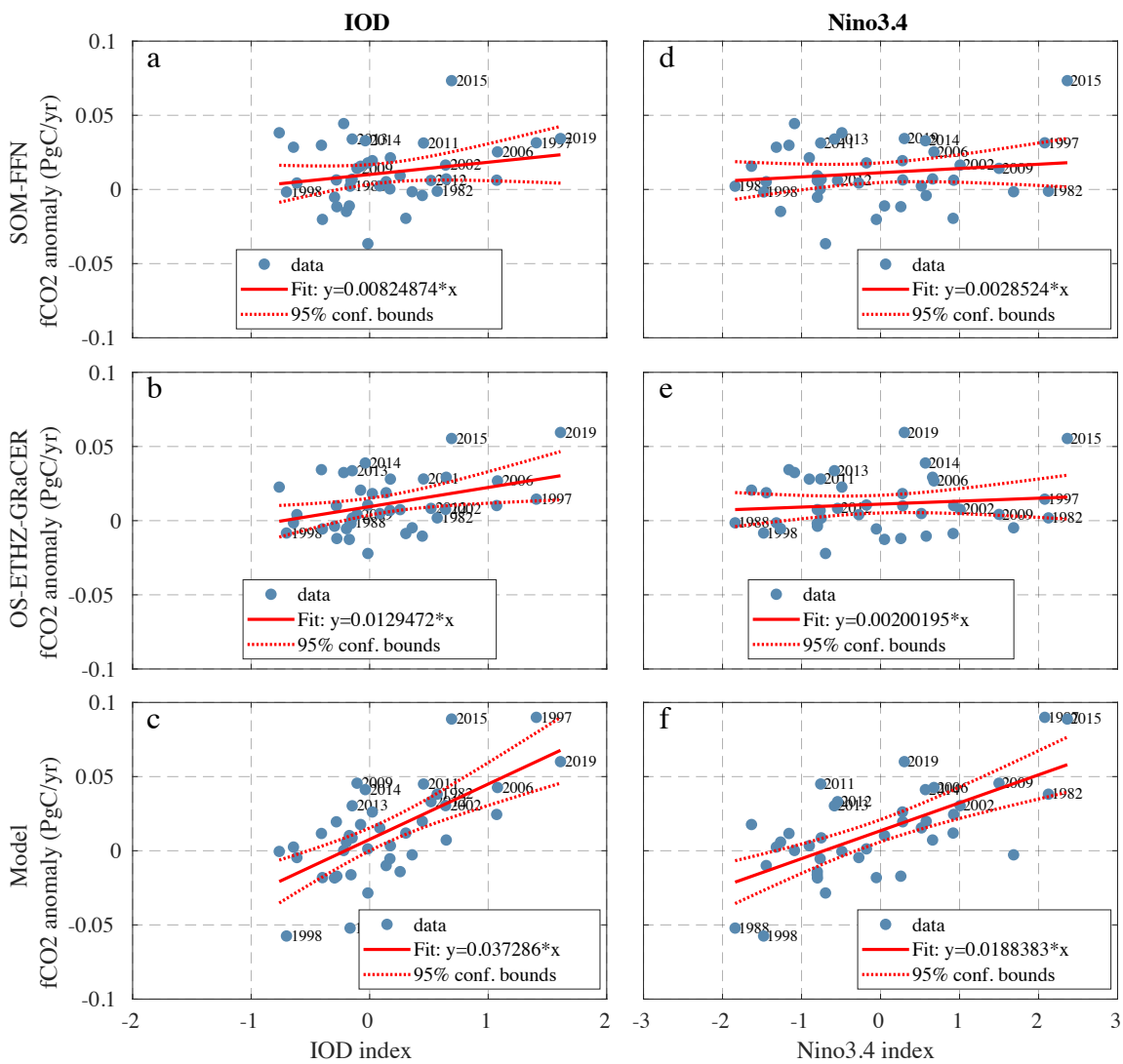


Fig. S2. The relation between CO<sub>2</sub> flux anomaly integrated in the Indian Ocean and index of IOD and Niño3.4 in two data products and model results. The two data products are from SOM-FFN and Niño3.4 in two data products and model results. As shown in this figure, the CO<sub>2</sub> flux anomaly in 2015 exhibits unique dynamics that are not fully captured by the conventional relationship between CO<sub>2</sub> flux anomaly and the IOD and Niño3.4 index.

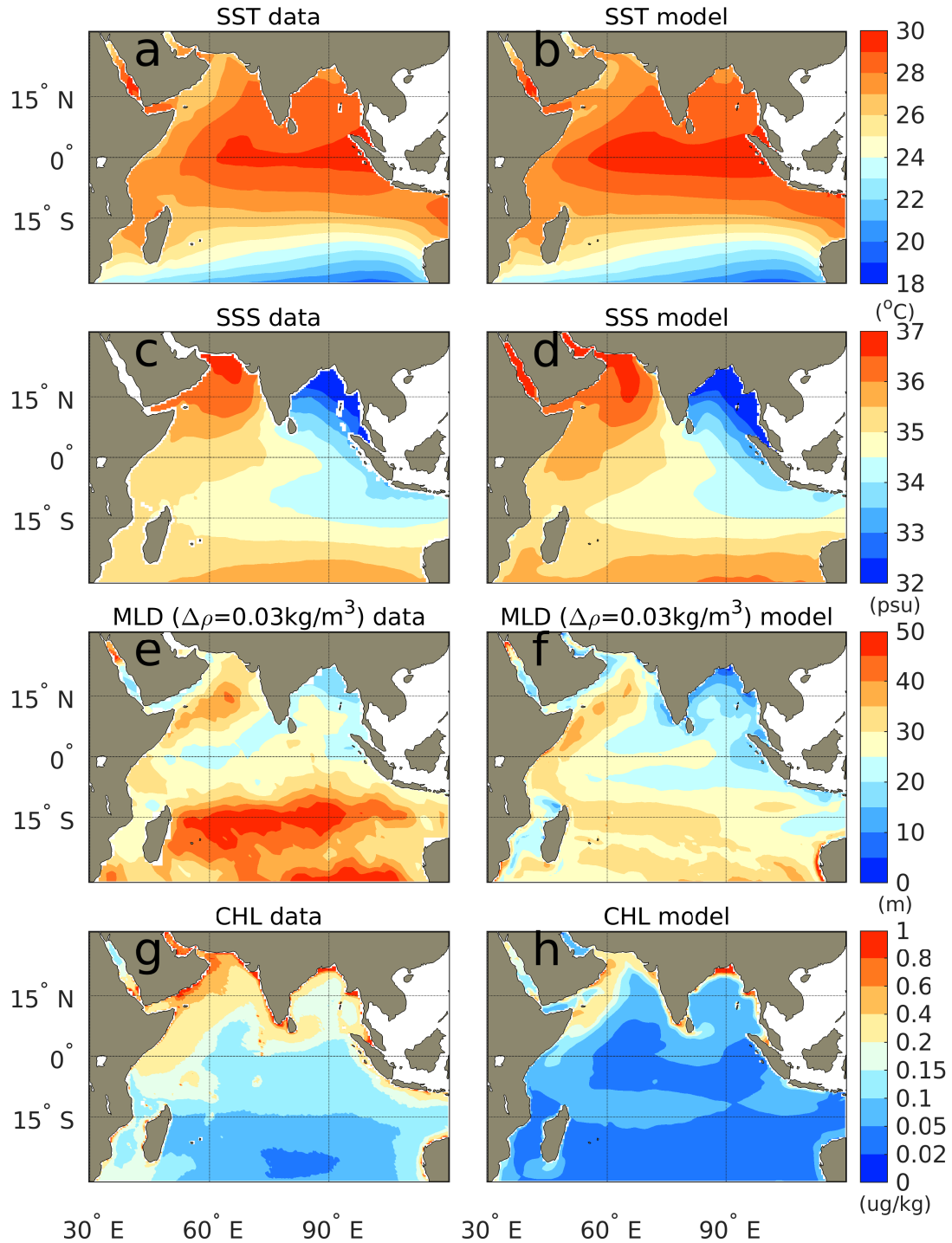


Fig. S3. Comparison of observed and simulated climatological annual mean of SST ( $^{\circ}\text{C}$ ), SSS (psu), mixing-layer depth (MLD, m), and surface chlorophyll ( $\text{ug/kg}$ ). Observed SST is from OISST v2, SSS from OISSL, MLD from de Boyer Montégut et al. (2004), chlorophyll from OC-CCI.

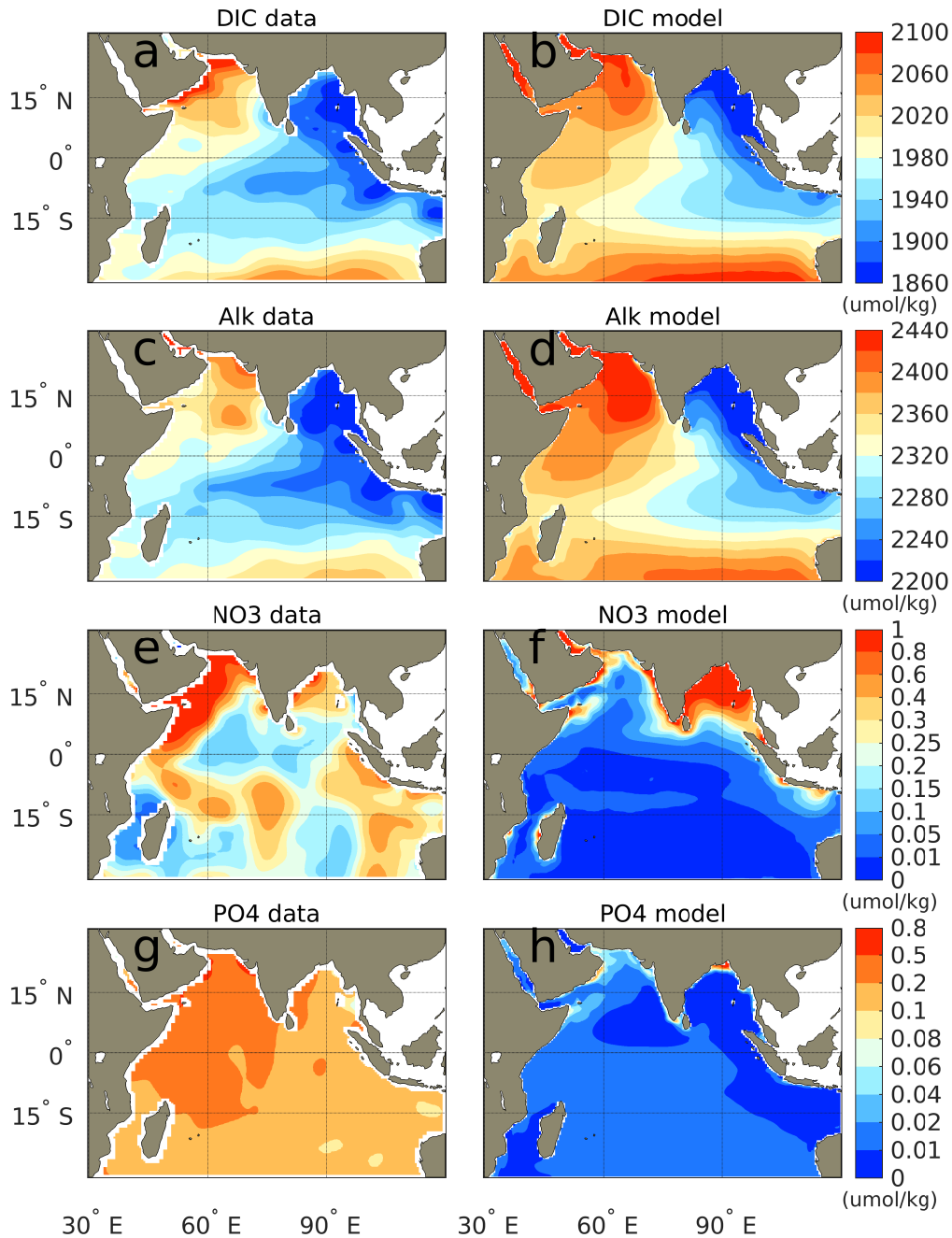


Fig. S4. Comparison of observed and simulated climatological annual mean of surface DIC (umol/kg), Alk (umol/kg), NO<sub>3</sub> (umol/kg), and PO<sub>4</sub> (umol/kg). Observed DIC and Alk are from GLODAP and NO<sub>3</sub> and PO<sub>4</sub> are from WOA 2013. The DIC in GLODAP is based on the year 2002. Under the consideration of anthropogenic carbon influence, the DIC annual mean is a mean between 1984 and 2020 where 2002 is the midpoint of 1984-2020. Therefore, the mean DIC in 1984-2020 and GLODAP DIC is comparable.

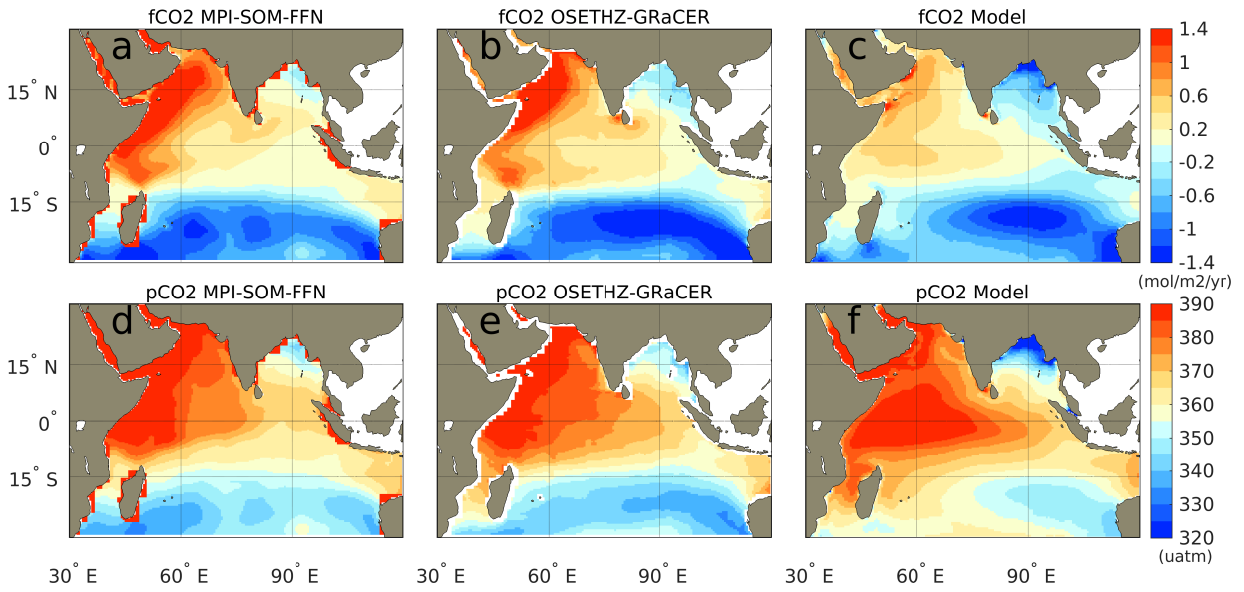


Fig. S5. Comparison of observed and simulated climatological annual mean of air-sea CO<sub>2</sub> flux (mol/m<sup>2</sup>/yr) and ocean pCO<sub>2</sub> (uatm). Observed CO<sub>2</sub> flux and ocean pCO<sub>2</sub> are from OS-ETHZ-GRaCER and SOM-FFN products. A positive flux denotes an outgassing from the ocean to atmosphere.

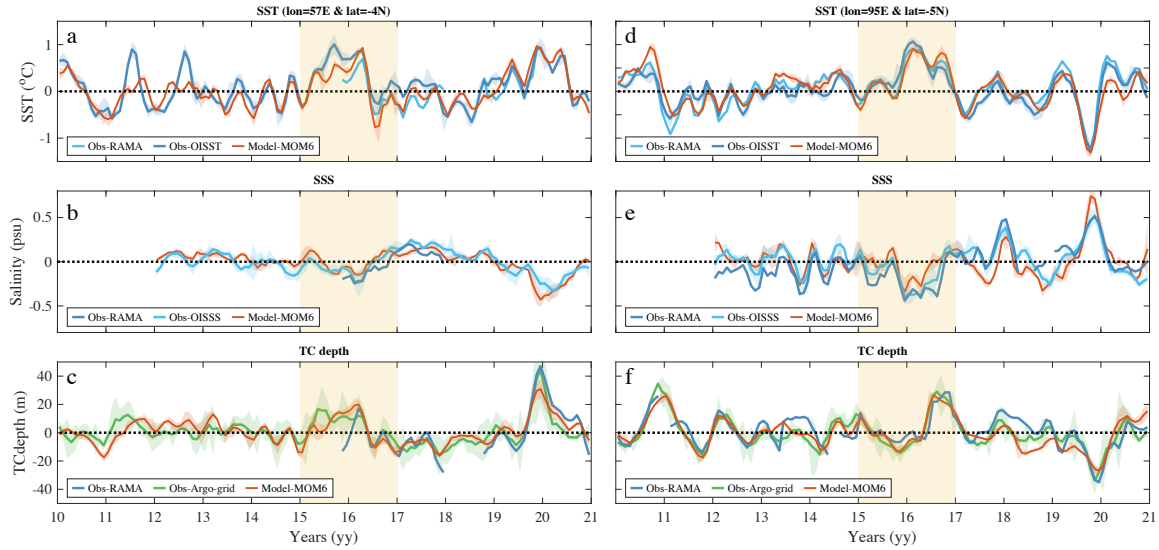


Fig. S6. Comparison of temporal evolution for SST ( $^{\circ}\text{C}$ ), SSS (psu), and thermocline depth (m) observed by RAMA station and simulated by model at two RAMA stations:  $57^{\circ}\text{E}$ ,  $4^{\circ}\text{S}$  and  $95^{\circ}\text{E}$ ,  $5^{\circ}\text{S}$ . The thermocline depth is defined as the depth at which the temperature reaches  $20^{\circ}\text{C}$ . Additional observations from the gridded satellite OISST, OISSS, and Argo float databases interpolated at the mooring location are also shown for evaluation. The yellow shading color highlights the specific period of interest (2015-2016) when the focused IOD occurs.

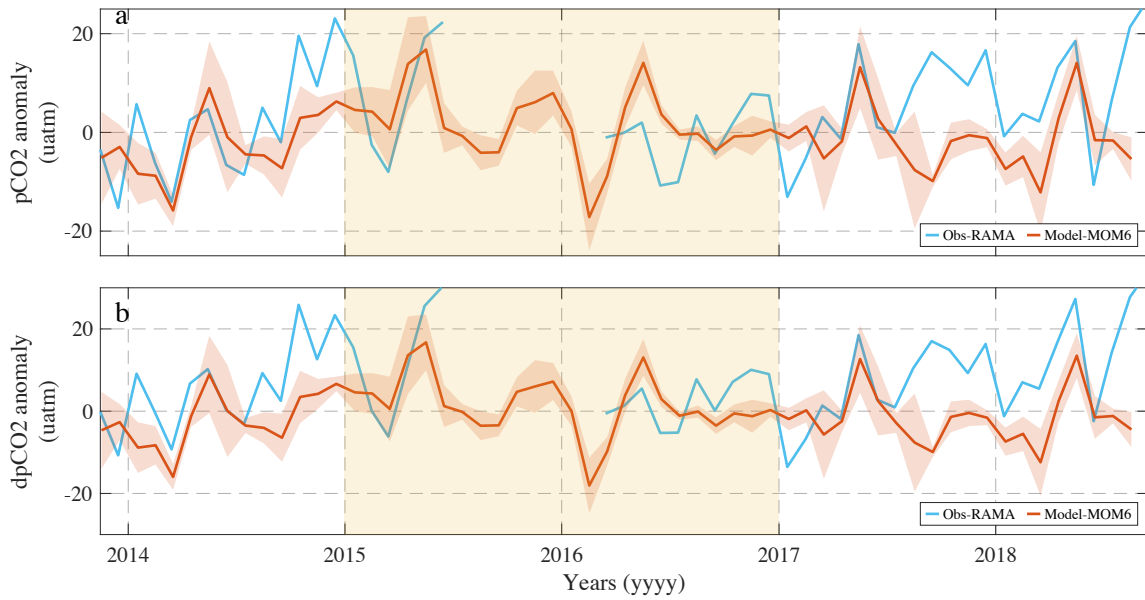


Fig. S7. Comparison of temporal evolution of anomalous ocean  $\text{pCO}_2$  and  $\Delta\text{pCO}_2$  (ocean-atmosphere  $\text{pCO}_2$  difference) observed by RAMA station and simulated by model at RAMA station ( $90^\circ\text{E}$ ,  $15^\circ\text{N}$ , Sutton et al., 2014). Due to the limited duration of observed data (2014-2019), the quadratically trend and climatological month value for anomaly computation are adopted from SOM-FFN data products. The yellow shading color highlights the specific period of interest (2015-2016) when the focused IOD occurs.

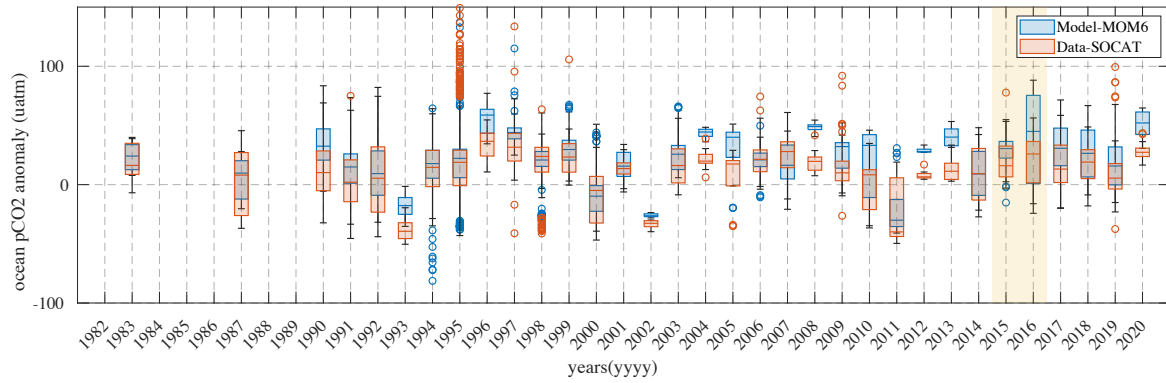


Fig. S8. The year-by-year box plot comparison of observed and simulated ocean CO<sub>2</sub> fugacity (fCO<sub>2</sub>) in the Indian Ocean during 1982-2020. The observed ocean CO<sub>2</sub> fugacity is collected from SOCAT monthly database. The simulated ocean pCO<sub>2</sub> is adjusted to fCO<sub>2</sub> and interpolated to match the SOCAT observational locations and times. The yellow shading color highlights the specific period of interest (2015-2016) when the focused IOD occurs.

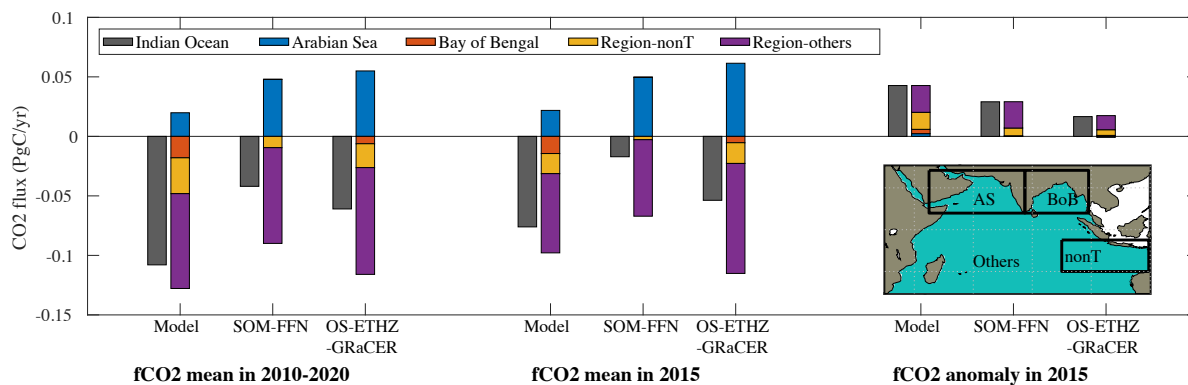


Fig. S9. The CO<sub>2</sub> flux integrated in the Indian Ocean and sub-regions computed as long-term annual mean (1982-2020), annual mean in 2015, and interannual anomaly in 2015. The sub-regions are defined in the map in the right-bottom bar plot. A positive flux denotes an outgassing from the ocean to atmosphere. As shown in this figure, the ocean CO<sub>2</sub> flux anomaly in 2015 is largely contributed by the region-others and NONT region.

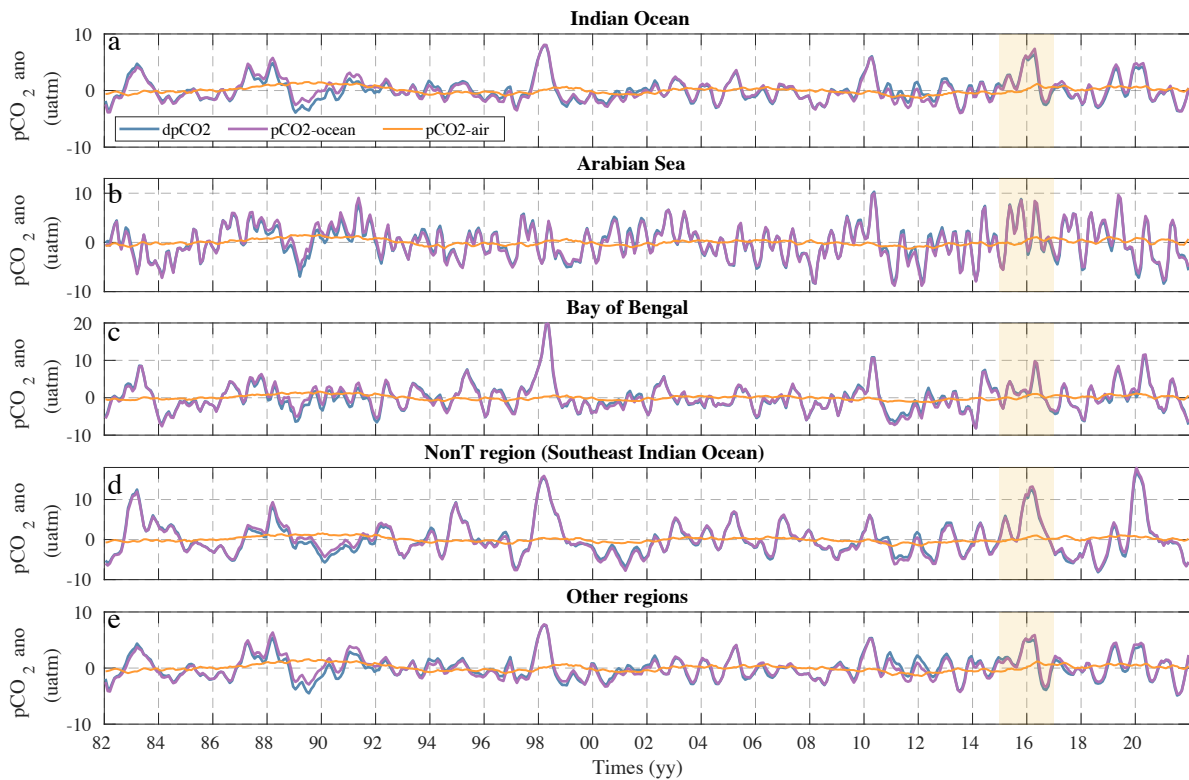


Fig. S10. Temporal evolution of anomalous ocean  $p\text{CO}_2$ , atmosphere  $p\text{CO}_2$ , and  $\Delta p\text{CO}_2$  (Ocean  $p\text{CO}_2$  minus atmosphere  $p\text{CO}_2$ ) averaged in the Indian Ocean (a), Arabian Sea (b), Bay of Bengal (c), NONT region (Southeastern Indian Ocean, d), and other regions (e). The atmospheric  $p\text{CO}_2$  is converted from  $x\text{CO}_2$  (GCB) with consideration of sea level pressure and water vapor in the MOM6-COBALT2. The ocean  $p\text{CO}_2$  and  $\Delta p\text{CO}_2$  are simulated by MOM6-COBALT2 forced by  $x\text{CO}_2$  (GCB). The yellow shading color highlights the specific period of interest (2015-2016) when the focused IOD occurs. See region definition in Fig. S9. As shown in this figure, the majority of  $\Delta p\text{CO}_2$  variability is controlled by the ocean  $p\text{CO}_2$ .

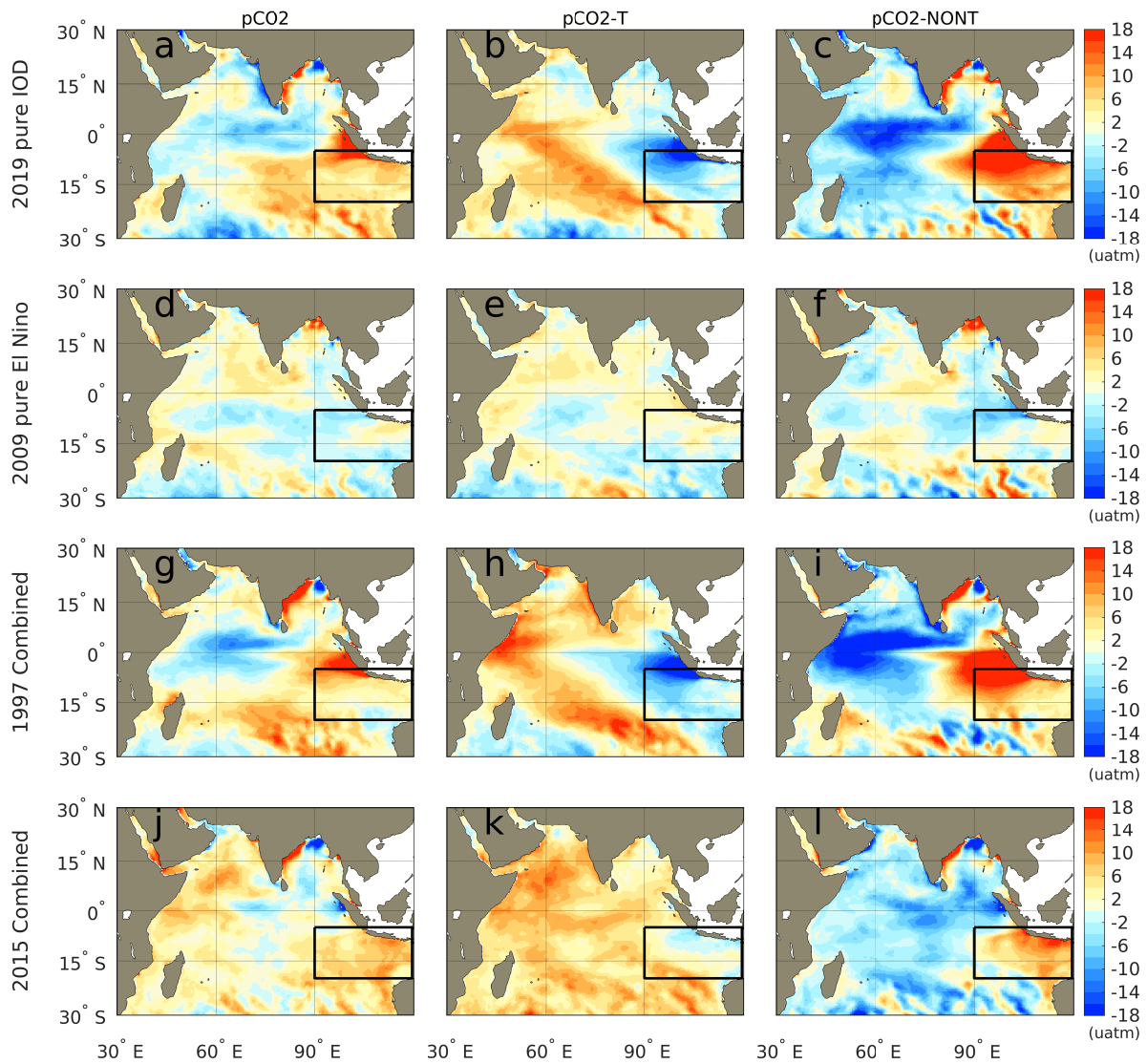


Fig. S11. Composited ocean pCO<sub>2</sub> anomaly and its two components: pCO<sub>2</sub>-T and pCO<sub>2</sub>-NONT averaged from August to January in the following year during different events: pure positive IOD (a-c), pure El Niño (d-f), combined positive IOD and El Niño in 1997 (g-i), and combined positive IOD and El Niño in 2015 (j-l). The ocean pCO<sub>2</sub> anomaly is decomposed into two components: pCO<sub>2</sub>-T and pCO<sub>2</sub>-NONT following Equation 2. As shown in this figure, the ocean pCO<sub>2</sub> anomaly and its two components exhibit a dipole anomaly pattern in the western and eastern Indian Ocean during the pure positive IOD and combined positive IOD and El Niño in 1997. There is a monopolar high ocean pCO<sub>2</sub> anomaly in the pure El Niño and combined positive IOD and El Niño in 2015.

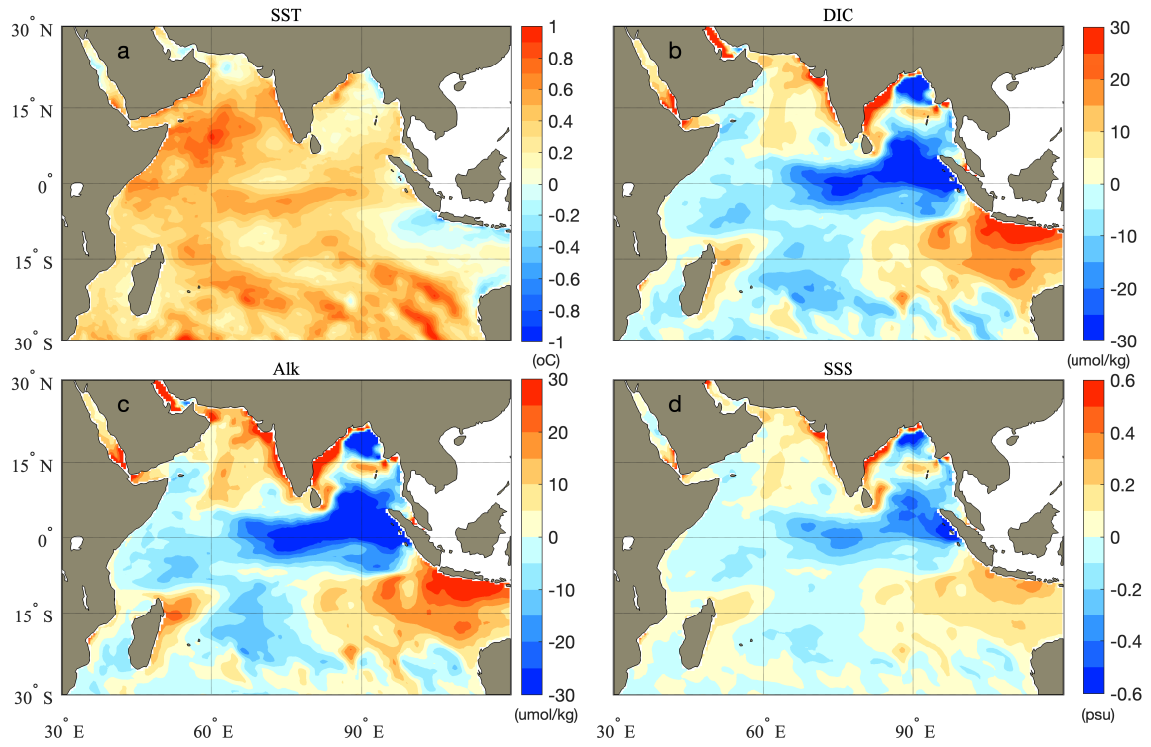


Fig. S12. Anomalous SST ( $^{\circ}\text{C}$ ), DIC ( $\mu\text{mol}/\text{kg}$ ), Alk ( $\mu\text{mol}/\text{kg}$ ), and SSS (psu) averaged from August 2015 to February 2016. As shown in this figure, there is an extensive warming in the western and central Indian Ocean and weakened cooling in the southeastern Indian Ocean. The DIC, Alk, and SSS increase anomalously in the southeastern Indian Ocean which is closely related to the Indonesian throughflow (ITF) anomaly.

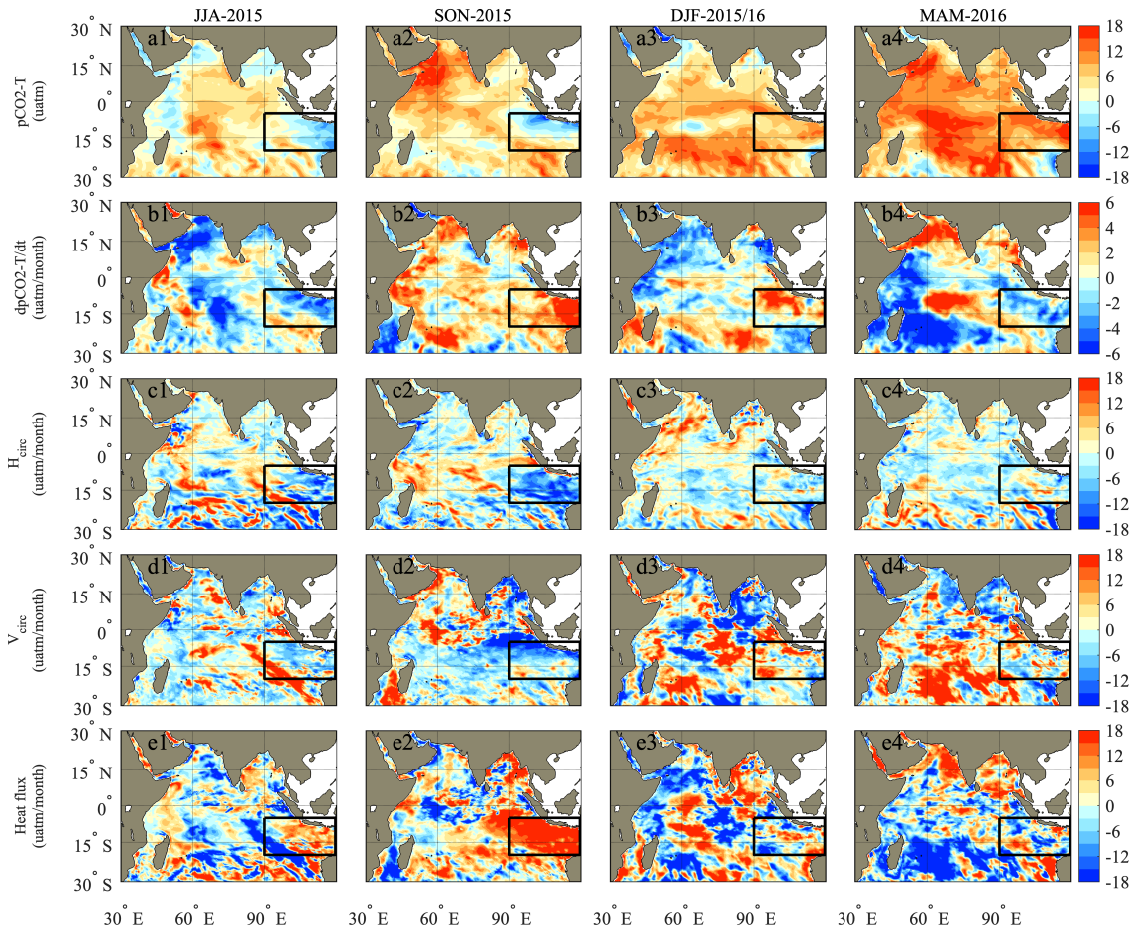


Fig. S13. The temporal evolution of  $p\text{CO}_2\text{-T}$  and diagnostic budget during the 2015 IOD. The panel is averaged every three months. The diagnostic budget is derived in Section S4.

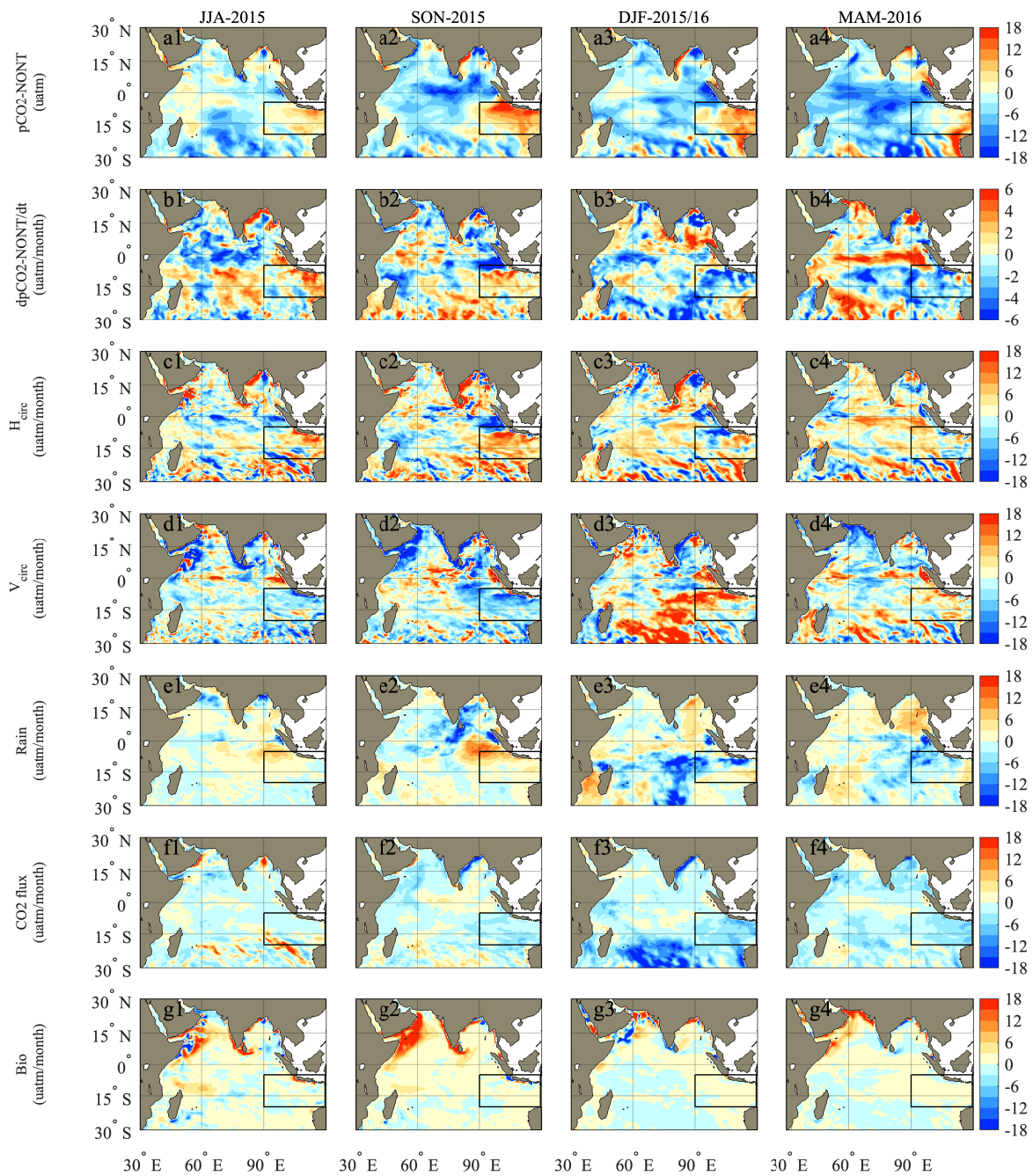


Fig. S14. Temporal evolution of pCO<sub>2</sub>-NONT and diagnostic budget during the 2015 IOD. The panel is averaged every three months. The diagnostic budget is derived in Section S4. Black box indicates the pCO<sub>2</sub>-NONT region.

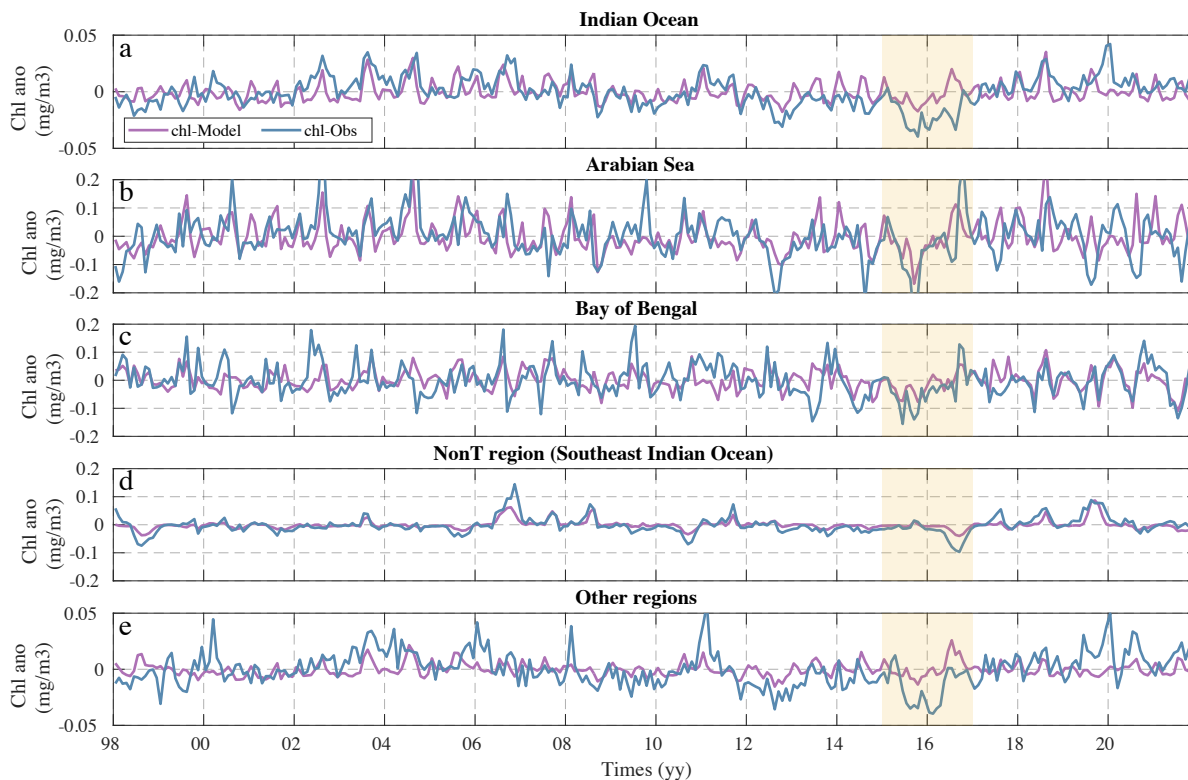


Fig. S15. Temporal evolution of anomalous chlorophyll between OC-CCI data and model in the Indian Ocean (a), Arabian Sea (b), Bay of Bengal (c), NONT region (southeastern Indian Ocean, d), other region (e). The yellow shading color highlights the specific period of interest (2015-2016) when the focused IOD occurs. See region definition in Fig. S9. As shown in this figure, the chlorophyll interannual variability in the southeastern Indian Ocean is lower than the variability in the Arabian Sea and Bay of Bengal. This indicates a weak influence of biology on the ocean  $p\text{CO}_2$  in the southeastern Indian Ocean.

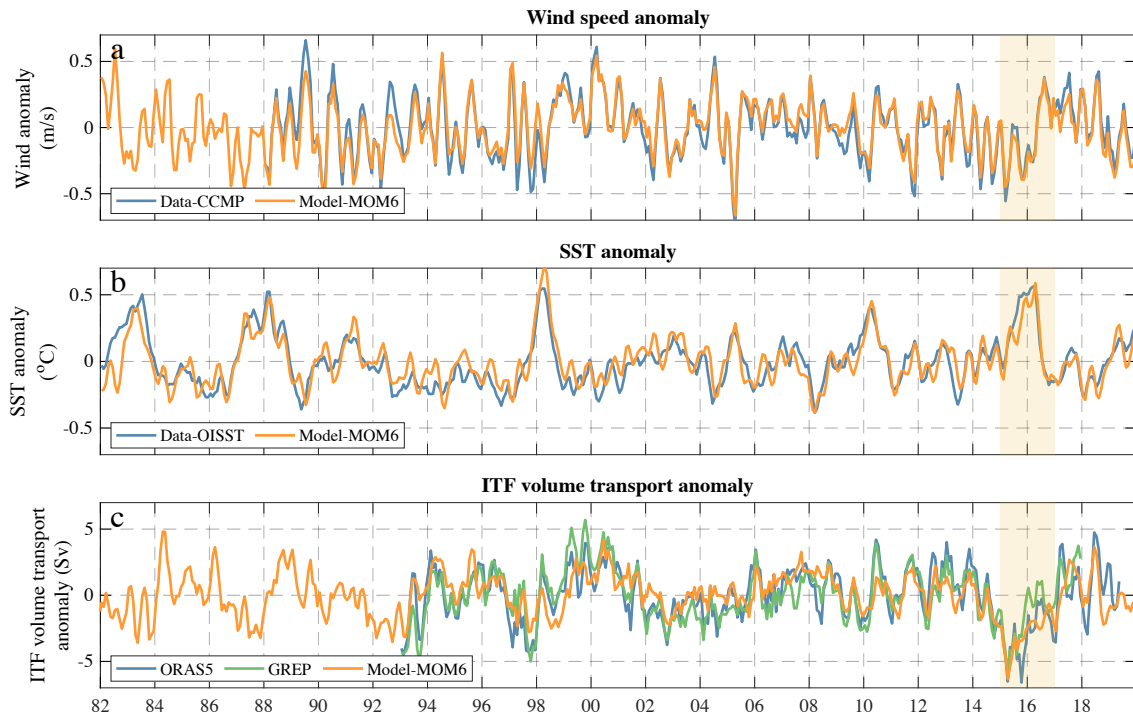


Fig. S16. Temporal evolution of anomalous wind speed, SST, and ITF volume transport in the Indian Ocean. The wind speed and SST are averaged in the Indian Ocean and ITF volume transport is computed at the Lombok Strait, Sunda Strait, and Timor passage connected to the Indian Ocean. The wind speed data is sourced from the CCMP product and JRA 55-do reanalysis product, SST is from OISST, and ITF volume transport is computed using GREP and ORAS5 ocean reanalysis product. The yellow shading color highlights the specific period of interest (2015-2016) when the focused IOD occurs. As shown in this figure, there is an extreme SST and ITF volume transport anomaly in 2015.

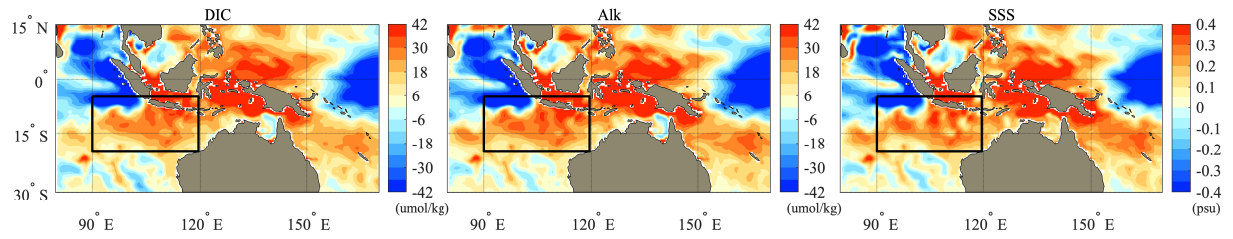


Fig. S17. Anomalous surface DIC, Alk, and salinity averaged in August 2015 and January 2016. The black box indicates the pCO<sub>2</sub>-NONT region, which is influenced by the ITF water of high ocean pCO<sub>2</sub> anomaly. As shown in this figure, the DIC, Alk, and SSS increase anomalously due to the departure of warm pool and reduced rainfall around the maritime continent.

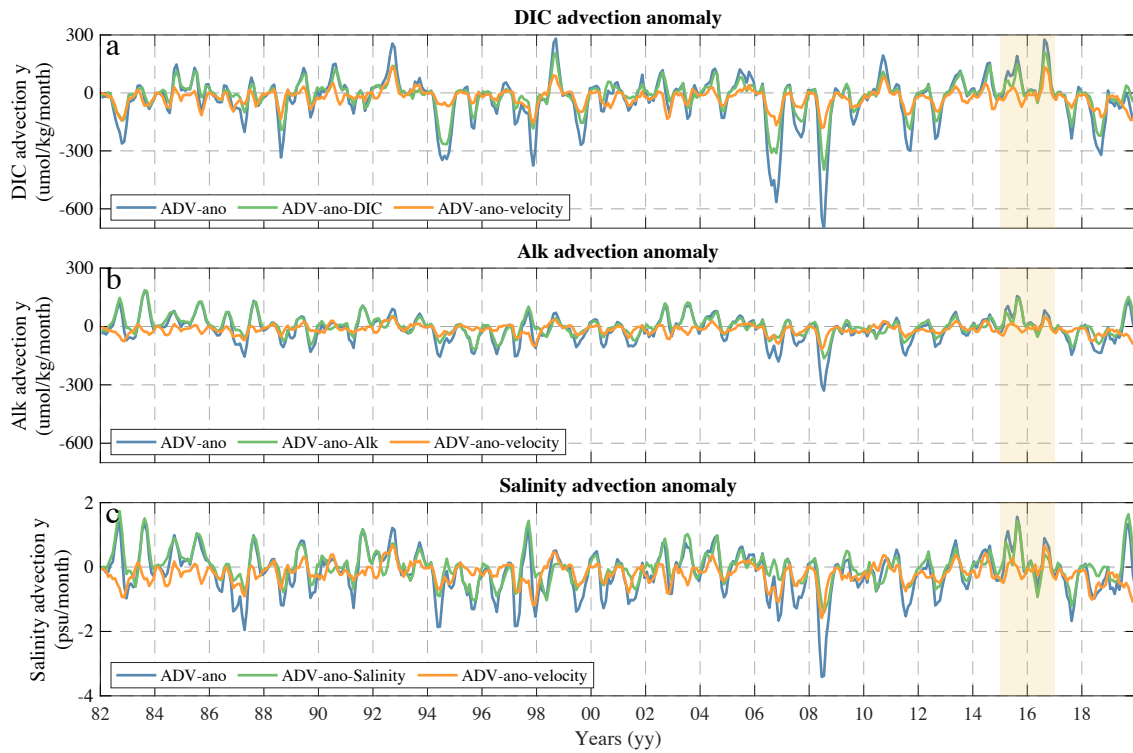


Fig. S18. Temporal evolution of DIC, Alk, and Salinity advection anomaly, along with its two components: advection anomaly due to concentration anomaly and advection anomaly due to velocity anomaly. The advection anomaly is weighted averaged at the Lombok Strait, Sunda Strait, and Timor passage by the volume transport. The yellow shading color highlights the specific period of interest (2015-2016) when the focused IOD occurs. As shown in this figure (panel a-c), most of advection anomaly is contributed by concentration anomaly during 2015 IOD.

## References

- Adcroft, A. and others 2019. The GFDL Global Ocean and Sea Ice Model OM4.0: Model Description and Simulation Features. *Journal of Advances in Modeling Earth Systems* **0**.
- Bakker, D. C. E. and others 2016. A multi-decade record of high-quality fCO<sub>2</sub> data in version 3 of the Surface Ocean CO<sub>2</sub> Atlas (SOCAT). *Earth System Science Data* **8**: 383-413.
- Banzon, V., T. M. Smith, T. M. Chin, C. Liu, and W. Hankins. 2016. A long-term record of blended satellite and in situ sea-surface temperature for climate monitoring, modeling and environmental studies. *Earth System Science Data* **8**: 165-176.
- de Boyer Montégut, C., G. Madec, A. S. Fischer, A. Lazar, and D. Iudicone. 2004. Mixed layer depth over the global ocean: An examination of profile data and a profile-based climatology. *Journal of Geophysical Research: Oceans* **109**.
- Doney, S. C. and others 2009. Mechanisms governing interannual variability in upper-ocean inorganic carbon system and air–sea CO<sub>2</sub> fluxes: Physical climate and atmospheric dust. *Deep Sea Research Part II: Topical Studies in Oceanography* **56**: 640-655.
- Feng, M., N. Zhang, Q. Liu, and S. Wijffels. 2018. The Indonesian throughflow, its variability and centennial change. *Geoscience Letters* **5**: 3.
- Friedlingstein, P. and others 2022. Global Carbon Budget 2022. *Earth Syst. Sci. Data* **14**: 4811-4900.
- Garcia, H. E. and others 2013a. World ocean atlas 2013. Volume 3, Dissolved oxygen, apparent oxygen utilization, and oxygen saturation, p. 25. *In* S. Levitus (Ed.) and A. V. Mishonov (Technical Ed.) [eds.]. NOAA Atlas NESDIS 75.
- Garcia, H. E. and others 2013b. World ocean atlas 2013. Volume 4, Dissolved inorganic nutrients (phosphate, nitrate, silicate), p. 25. *In* S. Levitus (Ed.) and A. V. Mishonov (Technical Ed.) [eds.]. NOAA Atlas NESDIS 76.
- Hu, S. and others 2019. Interannual to Decadal Variability of Upper-Ocean Salinity in the Southern Indian Ocean and the Role of the Indonesian Throughflow. *Journal of Climate* **32**: 6403-6421.
- Khatiwala, S. and others 2013. Global ocean storage of anthropogenic carbon. *Biogeosciences* **10**: 2169-2191.
- Kido, S., and T. Tozuka. 2017. Salinity Variability Associated with the Positive Indian Ocean Dipole and Its Impact on the Upper Ocean Temperature. *Journal of Climate* **30**: 7885-7907.
- Le Quéré, C., J. C. Orr, P. Monfray, O. Aumont, and G. Madec. 2000. Interannual variability of the oceanic sink of CO<sub>2</sub> from 1979 through 1997. *Global Biogeochemical Cycles* **14**: 1247-1265.
- Liao, E., L. Resplandy, J. Liu, and K. W. Bowman. 2020. Amplification of the Ocean Carbon Sink During El Niños: Role of Poleward Ekman Transport and Influence on Atmospheric CO<sub>2</sub>. *Global Biogeochemical Cycles* **34**: e2020GB006574.
- Locarnini, R. A. and others 2013. World ocean atlas 2013. Volume 1, Temperature, p. 40. *In* S. Levitus (Ed.) and A. V. Mishonov (Technical Ed.) [eds.]. NOAA Atlas NESDIS 73.
- Lovenduski, N. S., N. Gruber, S. C. Doney, and I. D. Lima. 2007. Enhanced CO<sub>2</sub> outgassing in the Southern Ocean from a positive phase of the Southern Annular Mode. *Global Biogeochemical Cycles* **21**.

- Mayer, M., M. Alonso Balmaseda, and L. Haimberger. 2018. Unprecedented 2015/2016 Indo-Pacific Heat Transfer Speeds Up Tropical Pacific Heat Recharge. *Geophysical Research Letters* **45**: 3274-3284.
- McKinley, G. A., M. J. Follows, and J. Marshall. 2004. Mechanisms of air-sea CO<sub>2</sub> flux variability in the equatorial Pacific and the North Atlantic. *Global Biogeochemical Cycles* **18**.
- McPhaden, M. J. and others 2009. RAMA: The Research Moored Array for African–Asian–Australian Monsoon Analysis and Prediction\*. *Bulletin of the American Meteorological Society* **90**: 459-480.
- Mears, C., T. Lee, L. Ricciardulli, X. Wang, and F. Wentz. 2022. Improving the Accuracy of the Cross-Calibrated Multi-Platform (CCMP) Ocean Vector Winds. *Remote Sensing*.
- Melnichenko, O., P. Hacker, J. Potemra, T. Meissner, and F. Wentz. 2021. Aquarius/SMAP sea surface salinity optimum interpolation analysis. IPRC Technical Note No 7.
- Montégut, C. d. B., G. Madec, A. S. Fischer, A. Lazar, and D. Iudicone. 2004. Mixed layer depth over the global ocean: An examination of profile data and a profile-based climatology. *Journal of Geophysical Research: Oceans* **109**.
- Najjar, R., and J. Orr. 1998. Design of OCMIP-2 simulations of chlorofluorocarbons, the solubility pump and common biogeochemistry. Internal OCMIP Report. LSCE/CEA Saclay.
- Obata, A., and Y. Kitamura. 2003. Interannual variability of the sea-air exchange of CO<sub>2</sub> from 1961 to 1998 simulated with a global ocean circulation-biogeochemistry model. *Journal of Geophysical Research: Oceans* **108**.
- Olsen, A. and others 2016. The Global Ocean Data Analysis Project version 2 (GLODAPv2) – an internally consistent data product for the world ocean. *Earth System Science Data* **8**: 297-323.
- Roemmich, D., and J. Gilson. 2009. The 2004–2008 mean and annual cycle of temperature, salinity, and steric height in the global ocean from the Argo Program. *Progress in Oceanography* **82**: 81-100.
- Sarmiento, J. L., and N. Gruber. 2006. *Ocean biogeochemical dynamics*. Princeton University Press.
- Sathyendranath, S. and others 2019. An Ocean-Colour Time Series for Use in Climate Studies: The Experience of the Ocean-Colour Climate Change Initiative (OC-CCI). *Sensors*.
- Stock, C. A. and others 2020. Ocean Biogeochemistry in GFDL's Earth System Model 4.1 and Its Response to Increasing Atmospheric CO<sub>2</sub>. *Journal of Advances in Modeling Earth Systems* **12**: e2019MS002043.
- Stock, C. A., J. P. Dunne, and J. G. John. 2014. Global-scale carbon and energy flows through the marine planktonic food web: An analysis with a coupled physical–biological model. *Progress in Oceanography* **120**: 1-28.
- Storto, A. and others 2019. The added value of the multi-system spread information for ocean heat content and steric sea level investigations in the CMEMS GREP ensemble reanalysis product. *Climate Dynamics* **53**: 287-312.
- Sutton, A. J. and others 2014. A high-frequency atmospheric and seawater pCO<sub>2</sub> data set from 14 open-ocean sites using a moored autonomous system. *Earth System Science Data* **6**: 353-366.
- Takahashi, T., J. Olafsson, J. G. Goddard, D. W. Chipman, and S. C. Sutherland. 1993. Seasonal variation of CO<sub>2</sub> and nutrients in the high-latitude surface oceans: A comparative study. *Global Biogeochemical Cycles* **7**: 843-878.

- Tsujino, H. and others 2018. JRA-55 based surface dataset for driving ocean–sea-ice models (JRA55-do). *Ocean Modelling* **130**: 79-139.
- Valsala, V., and S. Maksyutov. 2010. A Short Surface Pathway of the Subsurface Indonesian Throughflow Water from the Java Coast Associated with Upwelling, Ekman Transport, and Subduction. *International Journal of Oceanography* **2010**: 540783.
- Valsala, V., S. Maksyutov, and R. Murtugudde. 2010. Possible interannual to interdecadal variabilities of the Indonesian throughflow water pathways in the Indian Ocean. *Journal of Geophysical Research: Oceans* **115**.
- Wanninkhof, R. 2014. Relationship between wind speed and gas exchange over the ocean revisited. *Limnology and Oceanography: Methods* **12**: 351-362.
- Weiss, R. F., and B. A. Price. 1980. Nitrous oxide solubility in water and seawater. *Marine Chemistry* **8**: 347-359.
- Zhang, Y., Y. Du, and T. Qu. 2016. A sea surface salinity dipole mode in the tropical Indian Ocean. *Climate Dynamics* **47**: 2573-2585.
- Zuo, H., M. A. Balmaseda, S. Tietsche, K. Mogensen, and M. Mayer. 2019. The ECMWF operational ensemble reanalysis–analysis system for ocean and sea ice: a description of the system and assessment. *Ocean Sci.* **15**: 779-808.
- Zweng, M. M. and others 2013. World ocean atlas 2013. Volume 2, Salinity, p. 39. *In* S. Levitus (Ed.) and A. V. Mishonov (Technical Ed.) [eds.]. NOAA Atlas NESDIS 74.